Article | Received 27 August 2023; Accepted 18 October 2023; Published 23 October 2023
https://doi.org/10.55092/am20230002

3D Printed tandem X-Ray detector with halide perovskite-polymer composite semiconductor absorber

Haoran Li[1,2], Xin Shan[1,2], Shiran Bao[3,4], Sean Psulkowski[1,2], Wei Guo[3,4], Tarik Dickens[1,2], Zhibin Yu[1,2,*]

[1] Department of Industrial and Manufacturing Engineering, FAMU-FSU College of Engineering, Tallahassee FL 32310, USA
[2] High-Performance Materials Institute, Florida State University, Tallahassee FL 32310, USA
[3] Department of Mechanical Engineering, FAMU-FSU College of Engineering, Tallahassee FL 32310, USA
[4] National High Magnetic Field Laboratory, Tallahassee, Florida 32310, USA

* Correspondence author; E-mail: zyu@eng.famu.fsu.edu.

Abstract: A semiconductor-polymer composite was developed in this work consisting of inorganic halide perovskite ($CsPbBr_3$) crystals embedded in polylactic acid (PLA) matrix. The composite exhibits the essential semiconductor properties of $CsPbBr_3$ and the easy processability of PLA, enabling 3D printed tandem X-ray detectors. The tandem detectors demonstrated a sensitivity of 383 μC Gy_{air}^{-1} cm^{-2} when four layers and total 600 μm thick $CsPbBr_3$-PLA were printed. This sensitivity is 23X of single-layer detectors with same absorber thickness. The result indicates that 3D printed tandem detectors can overcome the X-ray absorption *vs.* charge carrier collection tradeoff in conventional single-layer detectors towards high performance radiation detection.

Keywords: 3D print; X-ray detector; halide perovskite; composite; tandem

1. Introduction

Digital imaging with X-ray detectors and detector arrays has important applications in medical diagnostics, security screening, and industrial nondestructive evaluation. Commonly, two methods are employed: indirect detection and direct detection. In indirect detection, high-energy X-ray photons are converted into low-energy visible photons through a scintillator absorber, while direct detection involves the conversion of X-ray photons into mobile electrical charges using a semiconductor absorber [1]. Direct detection can achieve a higher spatial resolution as compared to the indirect detection method due to the light scattering effect within the scintillator absorber, characteristic of indirect X-ray detectors [2–3]. However, direct X-ray detectors face challenges in efficiently collecting X-ray-induced

electrical charges, leading to the creation of additional charge trapping sites and a subsequent degradation of detector sensitivity over time [4]. This problem can become more severe when hard X-ray photons are used such that a thick semiconductor absorber layer in the detector for effective X-ray absorption is required. A large electrical field can be applied to accelerate the charge drifting process through the thick semiconductor absorber; however, this approach carries the risk of deteriorating the material and the detector's long-term stability due to potential electrical breakdown.

In the context of X-ray detectors utilizing a single semiconductor absorber layer, a dilemma arises as X-ray absorption and charge carrier collection are intricately linked. Improving one aspect often results in compromises on the other. On the other hand, a tandem X-ray detector, featuring multiple semiconductor absorber layers and charge collection terminals, offers a solution to disentangle such trade-offs [5]. The result is to optimize both X-ray absorption and charge carrier collection, enabling the sensitive detection of hard X-rays while operating under a low electrical field or voltage. Nonetheless, conventional semiconductor absorber materials, such as selenium (Se) and cadmium telluride (CdTe), are typically produced in high-vacuum enviro nments and/or at high processing temperatures, which restricts their scalability for manufacturing, impeding the realization of large-area, cost-effective multilayer tandem X-ray detectors and detector arrays [6–7].

Organometal halide perovskites have recently emerged as new semiconductor materials for radiation detection due to their high stopping power to high-energy X-ray photons and their extraordinary charge carrier transport properties [8]. Those materials can be dissolved in certain organic solvents and processed using various printing techniques to form crystalline thin films for large-area, cost-effective optoelectronic devices [9]. Moreover, it has been demonstrated that mixing the perovskite with a polymer matrix to form a perovskite-polymer composite has not deteriorated their optoelectronic properties in printed perovskite light-emitting diodes (LEDs) [10–11].

Processing thick perovskite films from a solution phase often leads to the formation of pinholes due to the low viscosity of the perovskite precursor solution and the use of high boiling point solvents (i.e., dimethylformamide, dimethyl sulfoxide, *etc*.) [12]. Embedded voids in the perovskite film can cause non-uniform electrical field distribution and premature electrical breakdown under X-ray irradiation, which could potentially lead to reliability issues in resulting perovskite X-ray detectors. Compared with pristine perovskites, the use of perovskite-polymer composites offers significantly improved manufacturing reliability and scalability. For instance, pinhole free composite films can be readily processed [13], and X-ray detectors could potentially be manufactured on a large scale, using spray coating, press molding, extrusion, and 3D printing *etc*. It is worth noting that 3D printing with polymer and polymer composite feedstocks has been recently implemented for multilayer integration of heterogeneous materials and functional devices [14]. In this work, we report 3D printed halide perovskite-polymer composites as semiconductor X-ray absorbers. The manufacturing flexibility of 3D printing enables the stacking of multiple layers of composite absorbers to realize tandem X-ray detectors. It has been demonstrated that the tandem detector displayed a consistent upward trend in photocurrent as the number and thickness of absorber layers

increased. This finding stands in stark contrast to the single-layer absorber detector, which exhibited a rapid decline in photocurrent as the absorber layer's thickness increased.

2. Methods

2.1. Materials

Cesium bromide (CsBr, 99.9%), lead bromide ($PbBr_2$, 99%), dimethyl sulfoxide (DMSO, anhydrous, 99.9%), toluene (anhydrous, 99.8%), dichloromethane (DCM, anhydrous, ≥99.8%, contains 40-150 ppm amylene as stabilizer) were purchased from Sigma-Aldrich. Polylactide resin 2003D (PLA) was purchased from Nature Works LLC. Conductive PLA filament was purchased from LulzBot. All materials were used as received.

2.2. Material preparation and characterizations

CsBr and $PbBr_2$ were mixed with 2:1 molar ratio and dissolved in DMSO with a concentration of 0.1 mmol/mL. The PLA resin was dissolved in DCM with a concentration of 150 mg/mL. 5ml of the perovskite precursor was slowly dropped into 300 mL toluene in 8 mins with sonication (QSONICA Sonicators) and settled for 5 hours to precipitate the $CsPbBr_3$ crystals. Those crystals were collected and washed two times with DCM. The PLA solution was mixed with $CsPbBr_3$ crystals with a desired weight ratio. The solution was then poured onto a cleaned glass substrate and dried on a hot plate at 80 ℃ for 1 hours. The dried film was peeled off from the glass substrate and used for material characterizations and X-ray detector fabrication. The perovskite-polymer composite filament was fabricated with a twin-screw extruder (Termo Scientific, HAAKE MiniLab II) at 180 ℃ and screw speed of 20 rpm. Field Emission SEM (JEOL-7401F), XRD (X'PERT Pro with Cu Kα radiation source), and a fluorometer (Horiba JY Fluoromax-4) were used to characterize the composite thin films.

2.3. Visible light and single-layer X-ray detector fabrication

The peeled off dried film was pressed at 180 ℃ by a Wabash hot press to obtain composite sheets with different thickness. A thin and transparent Au contact electrode and Mo_2O_3 were deposited in a vacuum thermal evaporator with a rate of 0.5 Å/s under 10^{-6} Torr. Ag contact electrode and C_{60} layer were evaporated on the other side with a rate of 2.0 Å/s and 0.5 Å/s under 10^{-6} Torr, respectively.

2.4. X-ray detector measurement

X-ray detection properties of the device were investigated using a standard fine-focus copper X-ray tube mounted in a Scintag PAD-V diffractometer, energized at 45 kV and 22.2 mA. The spectrum of the tube consists of a white background with cut-off at 45 keV, and the spectral lines of Cu K_α and K_β, as well as tungsten L-lines.

3. Result and discussion

Figure 1a shows a scanning electron microscopy (SEM) image of the as-synthesized $CsPbBr_3$, indicating a mixture of quasi-cuboid crystals and unfaceted particles with sizes from hundreds of nanometers to a few micrometers. Future exploration is worthwhile to optimize crystal synthesis with better controlled crystal shape, size, and size distribution to study their effects on composite formulation and device performance. Figure 1b shows the SEM image of one $CsPbBr_3$-PLA composite sample prepared by melt extrusion, indicating the uniform blending of the two components and a high compactness of the composite. Some $CsPbBr_3$ crystals appear to be elongated in the composite which can be caused by the shearing force at a high processing temperature during melt extrusion that deformed the crystals along the shearing direction. Figure 1c,d show the photos of one $CsPbBr_3$-PLA composite sheet in ambient light and under 365 nm UV light irradiation, respectively. The sample emits green light under UV, a characteristic of $CsPbBr_3$ with a direct bandgap of about 2.3 eV [15]. Figure 1e shows a photo of one $CsPbBr_3$-PLA composite filament. Both the composite sheet and the filament exhibit good uniformity throughout their sample areas, suggesting a good manufacturing reliability of the composite. The extruded composite filament was further used by a commercial LulzBot TAZ 6 3D printer with fused deposition modeling process. Figure 1f shows a top view photo of a 3D printed square. Figure 1g is a photo showing the side view of a stack of four 3D printed layers. An "FSU" pattern was also printed. Figure 1h shows a picture of the "FSU" sample under 365 nm UV light. The many different manufacturing processes that we demonstrated in this work can be advantageous for realizing low-cost and large area X-ray detectors with the $CsPbBr_3$-PLA composite.

The crystallinity of the composite film has been characterized by X-ray diffraction (XRD). As shown in Figure 2a, the film shows the characteristic diffraction peaks of cubic phase $CsPbBr_3$ with a lattice constant of 6.02 Å, which is in good agreement with literature results [16]. The photoluminescence (PL) and absorption spectra of the composite film were obtained as shown in Figure 2b. The PL spectrum displays an emission peak at around 535 nm, corresponding to a band gap of about 2.3 eV for the $CsPbBr_3$ crystals in the composite film. The PL spectrum has a full width at half maximum of 18 nm. An obvious transition in the absorption spectrum appears within 525 to 543 nm, consistent with the PL measurement. Figure 2c shows the tensile tests of the pristine PLA and $CsPbBr_3$-PLA composites with $CsPbBr_3$:PLA weight ratios of 2:1 and 4:1, respectively. The pristine PLA sample exhibits a Young's modulus of about 2.2 GPa, strain-to-failure of 4.8%, and tensile strength of 60 MPa. Incorporating $CsPbBr_3$ has noticeably improved the Young's modulus, while reducing the strain-to-failure. The 2:1 $CsPbBr_3$:PLA sample has a Young's modulus of 3.0 GPa, strain-to-failure of 3.4%, and tensile strength of 66 MPa. The 4:1 $CsPbBr_3$:PLA sample has a Young's modulus of 4.9 GPa, strain-to-failure of 0.7%, and tensile strength of 32 MPa. It appears that the 4:1 composite is very brittle, while the 2:1 composite has decent flexibility. Moreover, the 4:1 composite has a much higher viscosity at 180 °C than the 2:1 composite and could not produce uniform filament through extrusion. In this regard, we selected the 2:1 weight

ratio (equivalent to a volume percentage 34.8% of $CsPbBr_3$ in PLA) composite to continue the 3D printing and X-ray detector fabrication.

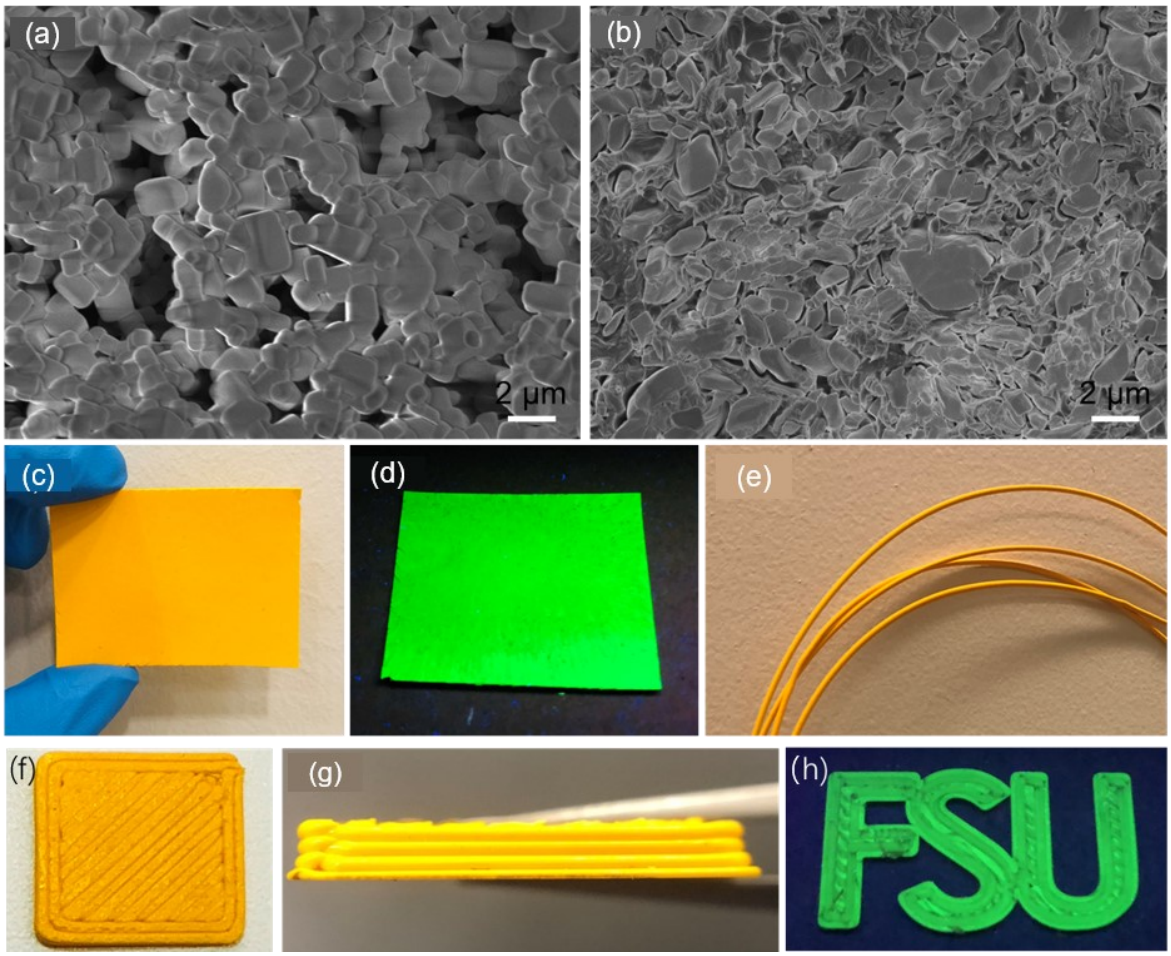

Figure 1. (a) A scanning electron microscopy (SEM) image of the as-synthesized perovskite crystals. **(b)** A SEM image of one $CsPbBr_3$-PLA (2:1) composite sample. **(c)** Photos of one $CsPbBr_3$-PLA (2:1) composite sheet in ambient light and **(d)** under 365 nm UV light illumination. **(e)** A photo of one $CsPbBr_3$-PLA (2:1) composite filament (~2.5 mm diameter) prepared by melt extrusion. **(f)** A top view photo of a 3D printed square. **(g)** A photo showing the side view of a stack of four 3D printed absorber layers. **(h)** A photo of one 3D printed "FSU" pattern under 365 nm UV light.

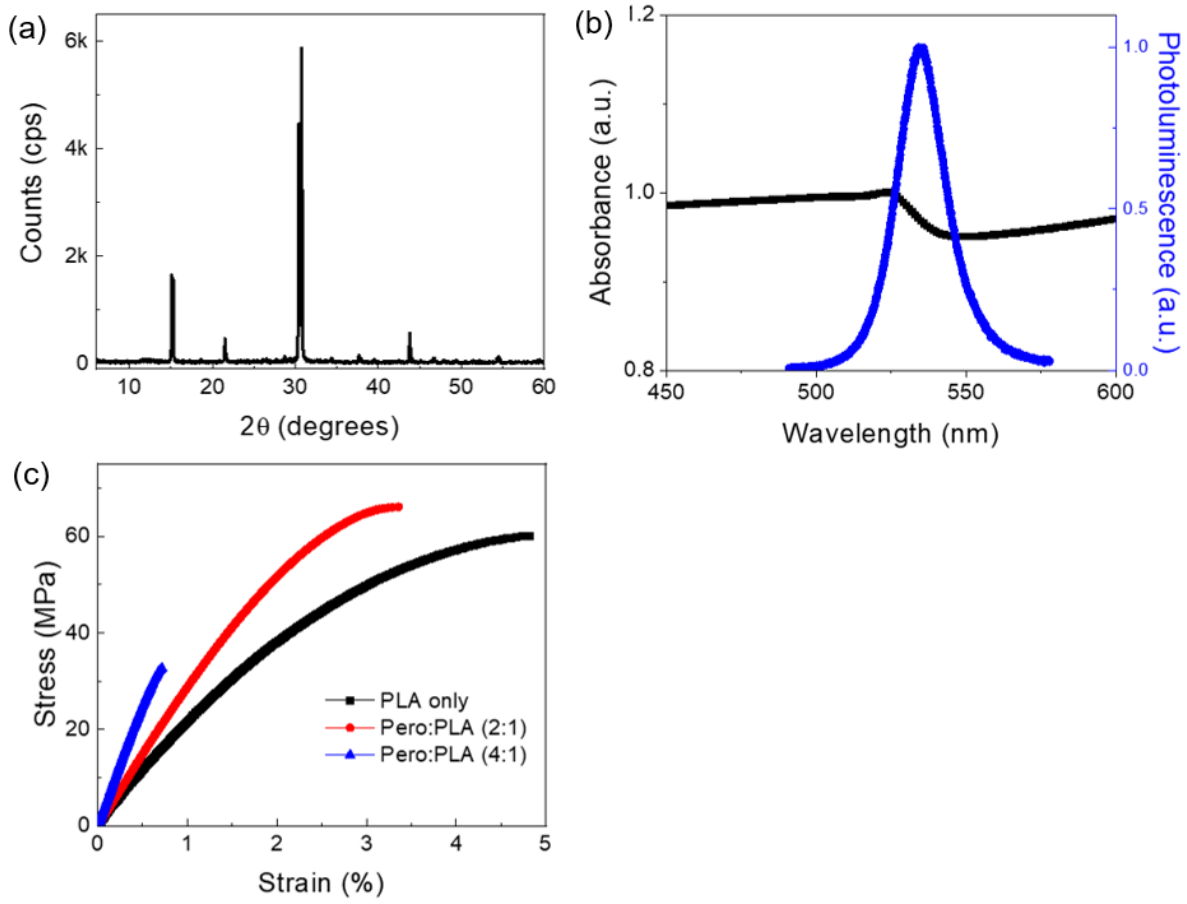

Figure 2. (a) X-ray diffraction (XRD) pattern of one $CsPbBr_3$-PLA (2:1) composite sample. **(b)** Photoluminescence (PL) and absorption spectra of one $CsPbBr_3$-PLA (2:1) composite. **(c)** Mechanical tensile tests of one pristine PLA and the indicated $CsPbBr_3$-PLA composite samples.

Drifting length ($\mu\tau E$, where μ is charge carrier mobility, τ is lifetime, and E is applied electric field) has been used to characterize how far a charge carrier (electron or hole) can travel through the absorber layer before recombination in a photodetector [17]. Its value limits the thickness of the absorber layer in the detector. A much larger absorber layer thickness than the drifting length can greatly reduce the charge carrier collection efficiency, leading to even lower detection sensitivity. In this regard, we continued to measure the drifting length values at different electrical fields for the 2:1 $CsPbBr_3$-PLA composite. Devices were fabricated with a structure as shown in Figure 3a. A vacuum evaporated gold (Au) thin film was used as the top contact, a thin layer of molybdenum oxide (Mo_2O_3) was used as the hole collection layer, a $CsPbBr_3$-PLA composite film as the light absorber, a layer of vacuum evaporated C_{60} thin film as the electric collection layer, and another layer of vacuum evaporated silver (Ag) as bottom contact. The top electrode was designed very thin (30 nm) to allow visible light to go through the electrode layer and absorbed by the perovskite-polymer absorber layer.

A blue LED was used as the light source to generate the electron-hole pairs in the perovskite composite film. Due to the strong absorption of the $CsPbBr_3$ to visible light, light

extinction and charge carrier generation would occur mostly within a very shallow depth close to the light incident surface. This argument is supported by Qaid *et al* [18], who reported that $CsPbBr_3$ had an absorption coefficient of 0.86×10^5 cm^{-1} near the band edge wavelength. This is to say that 116 nm thick $CsPbBr_3$ film will absorb 90% incident light Li et al [19] also reported that about 250 nm thick $CsPbBr_3$ layer had more than 80% absorbance to solar light. Therefore, the photocurrent in the $CsPbBr_3$-PLA device is determined by the drifting of electrons or holes towards the opposite electrode. By switching the polarity of the applied electrical field, the drifting length of electrons and holes can both be estimated from the photocurrent characteristics of the detectors following Equation (1) [20], where photocurrent is defined by the device current with light minus the current in dark, and A and B are arbitrary constants.

$$\text{Photocurrent}=A+B\times e^{\left(\frac{-\text{Absorber layer thickness}}{\text{Charge drifting length}}\right)} \quad (1)$$

Figure 3a shows the measurement setup for measuring electron drifting length, in which the charge carriers are generated on the top surface and the bottom electrode is positively biased to collect the drifting electrons. Figure 3b shows the photocurrent at different applied electrical fields for detectors with different absorber layer thickness. In all applied electrical fields, the photocurrent was found to exponentially decay with increasing absorber layer thickness. Electron drifting length was calculated from the slope of the fitting curve using Equation (1) and presented as in Figure 3c. Similar measurements were carried out as shown in Figure 3d-f to evaluate the hole drifting length at different electrical fields, where the bottom electrode was negatively biased for the drifting of holes. It appears that both electrons and holes exhibit increasing drifting length with increasing applied electric field. However, the electron drifting length shows a slight super-linear trend, while the hole drifting length has a slight sublinear trend with electric field. It is also observed that the electron drifting length remains slightly larger than the hole drifting length within the tested electric field range from 500 $V\cdot mm^{-1}$ to 1000 $V\cdot mm^{-1}$, for instance, the electron drifting length reaches 200 μm, while the hole drifting length is 143 μm when an electric field of 600 $V\cdot mm^{-1}$ is applied to the detector.

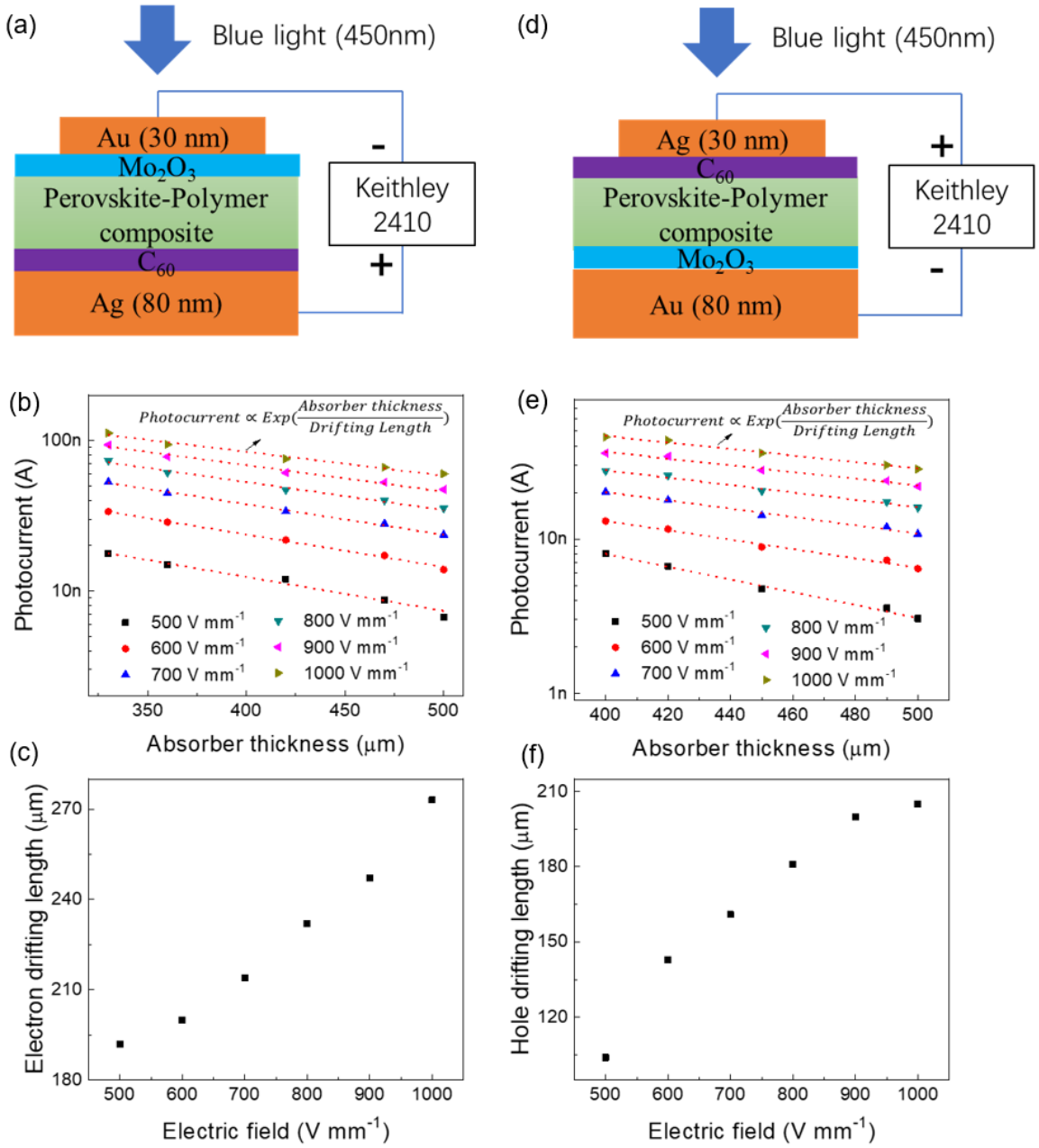

Figure 3. (a) Schematic drawing of the device structure and measurement setup for measuring electron drifting length. **(b)** Measured photocurrent at different applied electrical fields *vs.* different absorber thickness for electron drifting. **(c)** Calculated electron drifting length *vs.* applied electric field. **(d)** Schematic drawing of the device structure and measurement setup for measuring hole drifting length. **(e)** Measured photocurrent at different applied electrical fields *vs.* different absorber thickness for hole drifting. **(f)** Calculated hole drifting length *vs.* applied electric field.

X-ray detectors with a single layer of semiconductor absorber were characterized as shown in Figure 4a. The measurement setup is like the electron/hole drifting length measurements (Figure 3a,d) except that an X-ray source was used to replace the blue LED. X-ray irradiation was generated by a commercial X-ray tube. The X-ray dosage was

calibrated as 13.8 mGy_{air} s^{-1} using a Geiger counter. The average energy of the X-ray photons was calibrated by measuring their transmittance through $CsPbBr_3$-PLA (2:1) sheets with different thickness values. The samples were prepared by hot pressing. Transmitted X-ray photons were measured using a commercial silicon photodiode coupled CsI scintillator (Hamamatsu, S8559). The measurement result is shown in Figure S1a. A linear attenuation coefficient of 0.006 μm^{-1} is calculated that is equivalent to 60 cm^{-1}. In a 2:1 $CsPbBr_3$-PLA composite, the volume ratio of $CsPbBr_3$ is estimated to be 34.8%, given the densities of $CsPbBr_3$ and PLA are about 4.5 $g{\cdot}cm^{-3}$ and 1.2 $g{\cdot}cm^{-3}$ [21–22], respectively. Since X-ray photons are mostly absorbed by the $CsPbBr_3$ due to its much larger density than the PLA, the equivalent linear attenuation coefficient for $CsPbBr_3$ is 60/0.348=172.4 cm^{-1}, leading to a mass attenuation coefficient of 172.4/4.5=38.3 cm^2/g. According to documented literature of mass attenuation coefficient *vs.* X-ray photon energy in $CsPbBr_3$ (Figure S1b) [23], the average photon energy is about 23.6 keV for the X-ray source in our experiment.

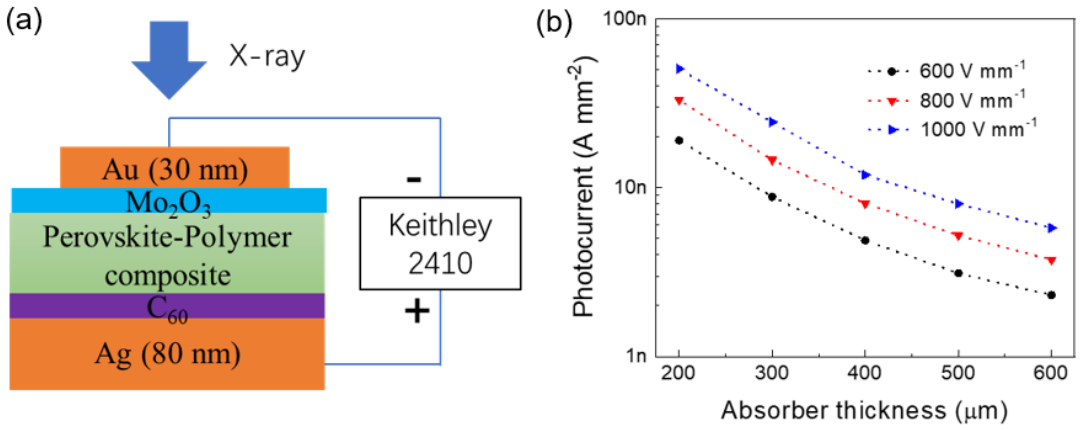

Figure 4. (a) Schematic drawing of the device structure and measurement setup for characterizing X-ray detectors with a single layer of $CsPbBr_3$-PLA absorber. **(b)** Measured photocurrent at different applied electrical fields *vs.* different absorber thickness.

X-ray induced photocurrents at different electric fields were recorded for detectors with different absorber layer thickness as shown in Figure 4b. It is observed that the photocurrent overall decreases with increasing absorber layer thickness. In contrast to the measurements in Figure 3, the photocurrent induced by X-ray cannot be well fitted with a one-phase exponential decay model. This difference can be caused by the following two aspects. Firstly, X-ray photons can penetrate deeper into the absorber layer. Both electron and hole drifting contribute to the photocurrent. Secondly, the enhanced X-ray absorption with increasing absorber layer can lead to more charge carrier generation in the detector that partially compensates for the exponential loss in charge carrier drifting efficiency. Nonetheless, it has been demonstrated that the drifting length limitation for both electrons (~ 200 μm) and holes (~ 150 μm) in the composite absorber had prevented achieving higher photocurrent and detection sensitivity by increasing absorber layer thickness.

According to the calculation in Figure 5a, a large absorber thickness is preferred to enhance X-ray absorption, especially when the incident X-ray photon energy increases. For instance, 500 μm thick $CsPbBr_3$-PLA (2:1) absorber can absorb about 95% of X-ray photons in our experiment in this work (average photon energy 23.6 keV); however, this same thickness would only absorb about 13% X-ray photons if the photon energy increases to 120 keV. High energy X-rays are often used for examination of dense objects, for instance, in interventional medical radiology and industrial nondestructive evaluation [24]. In those scenarios, the X-ray induced photocurrent in the $CsPbBr_3$-PLA detector will likely suffer by the tradeoff between absorption and charge carrier drifting.

To solve this problem, we have studied the plausibility of adopting a tandem device structure in which multiple detectors are vertically stacked in a parallel circuit connection. As shown in Figure 5b, we simulated the relative photocurrent responses of tandem detectors *vs.* the number of absorber layers according to Equation (2). I_1 is the photocurrent from the first detector on top and I_n is the total photocurrent from all the stacked detectors, and T is the transmittance of X-ray through a single absorber layer in the tandem detector assuming all sub-detectors have an identical absorber layer of 150 μm thick $CsPbBr_3$-PLA (2:1).

$$\mathbf{I_n}=I_1\times\left(1+T+...+T^{(n-1)}\right)=I_1\times\frac{1-T^n}{1-T} \qquad (2)$$

It is observed that the photocurrent gradually increases with increasing number of absorber layers if 23.6 keV X-ray irradiation is used; about 67% photocurrent improvement can be obtained if 5 absorber layers are used in the tandem detector comparing to a single absorber layer. The increasing trend becomes much faster and more significant if higher energy of X-ray irradiation is used. For 120 keV X-ray, 362% photocurrent improvement can be achieved for a tandem detector with 5 absorber layers.

To verify the above simulation, we fabricated tandem detectors using a commercial 3D printer, the $CsPbBr_3$-PLA (2:1) filament (Figure 1e) for the absorber layer, and a commercial graphite-PLA conductive filament (PROTOPASTA CDP12805) for the electrode terminals. The two filaments were printed by a LulzBot TAZ 6 printer with a dual extruder head. Figure 5c,d show photos of a 3D-printed tandem detector with two layers of $CsPbBr_3$-PLA absorber and three layers of graphite-PLA electrodes. The center of each layer is about 150 μm, while the edges of each layer appear much thicker because the printing feedstock piles up when the printing head makes stops at those locations. The 3D printed tandem detectors were characterized with 23.6 keV X-ray irradiation. Figure 5e shows the evolution of photocurrent when the number of 3D printed absorbers increased from 1 to 4 layers. An external bias of 90 V was applied between the two 3D-printed graphite-PLA electrodes on both sides of each absorber layer. The electric field is about 600 $V{\cdot}mm^{-1}$. The photocurrent started at about 29.8 $nA{\cdot}mm^{-2}$ if 1 layer was printed, increasing to 45.0 $nA{\cdot}mm^{-2}$, 50.6 $nA{\cdot}mm^{-2}$, and 52.9 $nA{\cdot}mm^{-2}$ for the 2-layer, 3-layer, and 4-layer tandem detectors, respectively. The measured trend is in good agreement with Figure 5b simulation (Figure S2). The slight offset between the measurement and simulation can be caused by thickness variation in the 3D-printed $CsPbBr_3$-PLA absorbers. It is worth noting that a single-layer detector with 600 μm thick absorber

would generate only 2.3 nA·mm^{-2} photocurrent at 600 V·mm^{-1} electric field, 23X lower than the tandem detector with 600 μm thick absorber (4 layers).

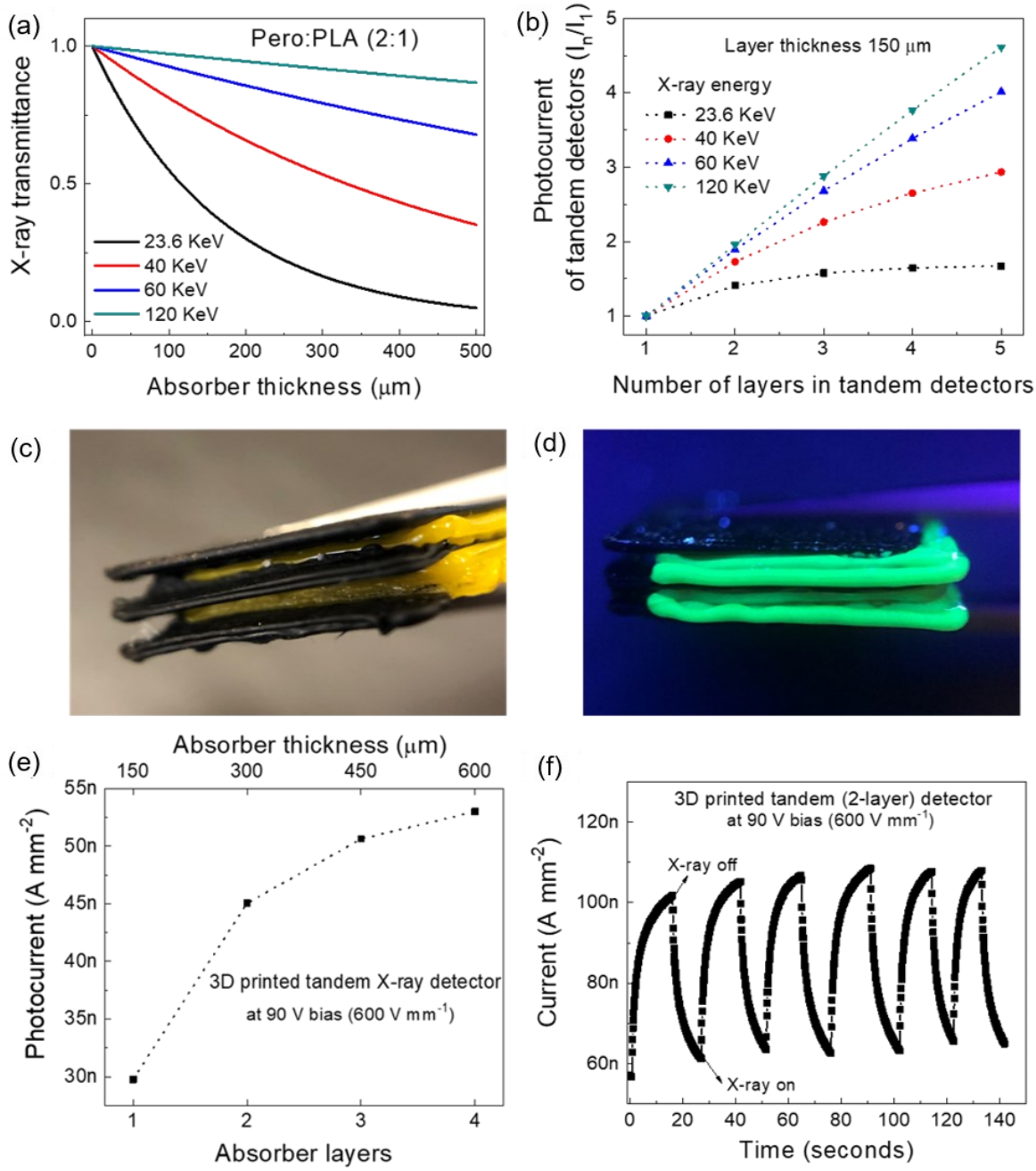

Figure 5. (a) Calculated transmittance of $CsPbBr_3$-PLA (2:1) absorber for X-ray photons with indicated energy *vs.* absorber thickness. **(b)** Simulated relative photocurrent responses to X-ray photons with indicated energy *vs.* the number of absorber layers in 3D printed tandem detectors. **(c)** Photos of a 3D-printed tandem detector with two layers of $CsPbBr_3$-PLA absorber and three layers of graphite-PLA in ambient light and **(d)** under 365 nm UV light illumination. **(e)** Evolution of photocurrent *vs.* absorber layers (thickness) in 3D printed tandem detectors. **(f)**

Transient responses of photocurrent with X-ray on and off for a 3D-printed, 2-layer tandem detector biased at 90 V.

Given the 13.8 mGy_{air} s^{-1} dosage of X-ray irradiation in our measurement, we calculated the sensitivities of our 3D printed detectors as 216 μC Gy_{air}^{-1} cm^{-2}, 326 μC Gy_{air}^{-1} cm^{-2}, 367 μC Gy_{air}^{-1} cm^{-2}, and 383 μC Gy_{air}^{-1} cm^{-2}, with 1-layer, 2-layer, 3-layer, and 4-layer $CsPbBr_3$-PLA absorbers, respectively. Those values are low compared to reported spectroscopic-grade $CsPbBr_3$ single crystals by He *et al* that exhibited a sensitivity of 5,111 μC Gy_{air}^{-1} cm^{-2} to 50 keV_{peak} X-ray irradiation [25]. Nonetheless, the advantages of low-cost formulation and manufacturing flexibility of the $CsPbBr_3$-PLA composites can benefit the exploration of new device architectures (tandem detectors and pixelated detector arrays, *etc*.) using 3D printing. It is also argued that the above sensitivity gap can be less significant when more energetic X-ray irradiation is used, due to the decoupling of X-ray absorption and charge carrier drifting in the 3D-printed tandem detectors.

Figure 5f shows the transient responses of photocurrent for a 3D-printed, 2-layer tandem detector that was biased at 90 V. The measured current experienced a relatively slow rise and fall, taking about 5-10 seconds to reach over 75% of total changes. Also, the dark current measured when the X-ray source was shut off shows a slightly increasing trend over measurement time. These two problems can be caused by charge trapping effects due to electronic and ionic defects at the $CsPbBr_3$ and PLA interfaces [26]. Future work is needed to reduce the density of electronic and ionic defects, for example, by introducing appropriate surface functionalization for the $CsPbBr_3$ crystals [27]. While this current work focuses on process development and device demonstration, future exploration is also demanded to investigate the durability of the 3D printed detectors upon beam damage by both soft and hard X-ray photons.

4. Conclusion

We have developed $CsPbBr_3$ and PLA composites as semiconductor absorbers for X-ray detectors. With 2:1 weight ratio of $CsPbBr_3$ to PLA, the composite preserves the good mechanical properties comparable to the pristine PLA, exhibiting a Young's modulus of 3.0 GPa, tensile strength of 66 MPa, and strain-to-failure of 3.4%. Like PLA and other commodity plastics, the $CsPbBr_3$-PLA (2:1) composite can be processed into different shapes and sizes using hot pressing, extrusion, and 3D printing. At the same time, the composite shows the essential optoelectronic properties of $CsPbBr_3$ crystals including charge carrier generation and drifting upon photoexcitation. The measured electron drifting length is about 200 μm and hole drifting length is about 143 μm at 600 V mm^{-1} applied electric field in the $CsPbBr_3$-PLA (2:1) composite. 3D printed tandem X-ray detectors have also been demonstrated with different layers of $CsPbBr_3$-PLA absorber. The detection sensitivity reaches 216 μC Gy_{air}^{-1} cm^{-2}, 326 μC Gy_{air}^{-1} cm^{-2}, 367 μC Gy_{air}^{-1} cm^{-2}, and 383 μC Gy_{air}^{-1} cm^{-2} at 600 V mm^{-1} with 1-layer, 2-layer, 3-layer, and 4-layer 3D printed absorbers, respectively. This result indicates that 3D printed tandem detectors can break the X-ray absorption *vs.* charge carrier collection tradeoff in conventional single-layer detectors for achieving more sensitive radiation

detection. The overall composite formulation and 3D printing process in this work can be more generally employed in future to address challenges in integration of dissimilar electronic materials for complex structures and novel functions.

5. Supplementary data

The authors confirm that the supplementary data are available within this article.

Acknowledgements

The work is financially supported by the National Science Foundation under award #2302478 and the NNSA Minority Serving Institution Partnership Program (MSIPP) under award #DE-NA0004004.

Conflicts of Interests

No conflicts of interest were reported by any of the authors.

References

[1] Yaffe MJ, Rowlands JA. X-ray detectors for digital radiography. *Phys Med Biol* 1997, 42(1):1-39.

[2] Kim BJ, Cha BK, Jeon H, Chi YK, Cho G. A study on spatial resolution of pixelated CsI(Tl) scintillator. *Nucl Instrum Meth A* 2007, 579(1):205-207.

[3] Que W, Rowlands JA. X-Ray-Imaging using amorphous selenium - inherent spatial-resolution. *Med Phys* 1995, 22(4):365-374.

[4] Strassburg M, Schroeter C, Hackenschmied P. CdTe/CZT under high flux irradiation. *J Instrum* 2011, 6:C01055.

[5] Redus R, Huber A, Pantazis J, Pantazis T, Takahashi T, *et al*. Multielement CdTe stack detectors for gamma-ray spectroscopy. *IEEE T Nucl Sci* 2004, 51(5):2386-2394.

[6] Del Sordo S, Abbene L, Caroli E, Mancini AM, Zappettini A, *et al*. Progress in the development of CdTe and CdZnTe semiconductor radiation detectors for astrophysical and medical applications. *Sensors-Basel* 2009, 9(5):3491-3526.

[7] Farahmandzadeh M, Marcinko S, Jaramillo C, Cheng MK, Curreli D, *et al*. Simulation and experimental validation of the uniformity of thermally evaporated amorphous selenium films for large-area imaging and radiation detection applications. *IEEE T Electron Dev* 2021, 68(2):626-631.

[8] Wei HT, Huang JS. Halide lead perovskites for ionizing radiation detection. *Nat Commun* 2019, 10:1066.

[9] Stranks SD, Snaith HJ. Metal-halide perovskites for photovoltaic and light-emitting devices. *Nat Nanotechnol* 2015, 10(5):391-402.

[10] Li JQ, Bade SGR, Shan X, Yu ZB. Single-layer light-emitting diodes using organometal halide perovskite/poly(ethylene oxide) composite thin films. *Adv Mater* 2015, 27(35):5196-5202.

[11] Bade SGR, Li JQ, Shan X, Ling YC, Tian Y, *et al*. Fully printed halide perovskite light-emitting diodes with silver nanowire electrodes. *ACS Nano* 2016, 10(2):1795-1801.
[12] Kim YC, Kim KH, Son DY, Jeong DN, Seo JY, *et al*. Printable organometallic perovskite enables large-area, low-dose X-ray imaging. *Nature* 2017, 550(7674):87-91.
[13] Li HR, Shan X, Neu JN, Geske T, Davis M, *et al*. Lead-free halide double perovskite-polymer composites for flexible X-ray imaging. *J Mater Chem C* 2018, 6(44):11961-11967.
[14] Loke G, Yuan R, Rein M, Khudiyev T, Jain Y, *et al*. Structured multimaterial filaments for 3D printing of optoelectronics. *Nat Commun* 2019, 10:4010.
[15] Mannino G, Deretzis I, Smecca E, La Magna A, Alberti A, *et al*. Temperature-dependent optical band gap in $CsPbBr_3$, $MAPbBr_3$, and $FAPbBr_3$ single crystals. *J Phys Chem Lett* 2020, 11(7):2490-2496.
[16] Stoumpos CC, Malliakas CD, Peters JA, Liu ZF, Sebastian M, *et al*. Crystal growth of the perovskite semiconductor $CsPbBr_3$: a new material for high-energy radiation detection. *Cryst Growth Des* 2013, 13(7):2722-2727.
[17] Zanichelli M, Santi A, Pavesi M, Zappettini A. Charge collection in semi-insulator radiation detectors in the presence of a linear decreasing electric field. *J Phys D Appl Phys* 2013, 46(36):365103.
[18] Qaid SMH, Ghaithan HM, Al-Asbahi BA, Aldwayyan AS. Achieving optical gain of the $CsPbBr_3$ perovskite quantum dots and influence of the variable stripe length method. *ACS Omega* 2021, 6(8):5297-5309.
[19] Li X, Tan Y, Lai H, Li SP, Chen Y, *et al*. All-inorganic $CsPbBr_3$ perovskite solar cells with 10.45% efficiency by evaporation-assisted deposition and setting intermediate energy levels. *ACS Appl Mater Inter* 2019, 11(33):29746-29752.
[20] Tchernycheva M, Neplokh V, Zhang H, Lavenus P, Rigutti L, *et al*. Core-shell InGaN/GaN nanowire light emitting diodes analyzed by electron beam induced current microscopy and cathodoluminescence mapping. *Nanoscale* 2015, 7(27):11692-11701.
[21] Barrasa JO, Ferrandez-Montero A, Ferrari B, Pastor JY. Characterisation and modelling of PLA filaments and evolution with time. *Polymers-Basel* 2021, 13(17):2899.
[22] Bruzzi M, Talamonti C. Characterization of crystalline $CsPbBr_3$ perovksite dosimeters for clinical radiotherapy. *Front Phys-Lausanne* 2021, 9:625282.
[23] Photon cross section database now available on-line. *J Res Natl Inst Stan* 1998, 103(2):249-249.
[24] Datta A, Zhong Z, Motakef S. A new generation of direct X-ray detectors for medical and synchrotron imaging applications. *Sci Rep-Uk* 2020, 10(1):20097.
[25] He YH, Hadar I, De Siena MC, Klepov VV, Pan L, *et al*. Sensitivity and detection limit of spectroscopic-grade perovskite $CsPbBr_3$ crystal for hard X-Ray detection. *Adv Funct Mater* 2022, 32(24):2112925.
[26] Shao YH, Xiao ZG, Bi C, Yuan YB, Huang JS. Origin and elimination of photocurrent hysteresis by fullerene passivation in $CH_3NH_3PbI_3$ planar heterojunction solar cells. *Nat Commun* 2014, 5:5784.
[27] Pothoof J, Westbrook RJE, Giridharagopal R, Breshears MD, Ginger DS. Surface

passivation suppresses local ion motion in halide perovskites. *J Phys Chem Lett* 2023, 14(26):6092-6098.